

Transport signatures of relativistic quantum scars in a graphene cavityG. Q. Zhang,^{1,*} Xianzhang Chen,^{2,*} Li Lin,³ Hailin Peng,³ Zhongfan Liu,³ Liang Huang,^{2,†} N. Kang^{⊗,1,‡} and H. Q. Xu^{1,4,§}¹*Beijing Key Laboratory of Quantum Devices, Key Laboratory for the Physics and Chemistry of Nanodevices, and Department of Electronics, Peking University, Beijing 100871, People's Republic of China*²*School of Physical Science and Technology and Key Laboratory for Magnetism and Magnetic Materials of MOE, Lanzhou University, Lanzhou, Gansu 730000, People's Republic of China*³*Center for Nanochemistry, Beijing Science and Engineering Center for Nanocarbons, Beijing National Laboratory for Molecular Sciences, College of Chemistry and Molecular Engineering, Peking University, Beijing 100871, People's Republic of China*⁴*Beijing Academy of Quantum Information Sciences, Beijing 100193, People's Republic of China*

(Received 25 August 2019; accepted 13 January 2020; published 5 February 2020)

Wave function scars refer to localized complex patterns of enhanced wave function probability distributions in a quantum system. Existing experimental studies of wave function scars concentrate nearly exclusively on nonrelativistic quantum systems. Here we present a combined experimental and theoretical study of a relativistic quantum cavity system realized by etching a graphene sheet. The conductance of the graphene cavity has been measured as a function of the back gate voltage (or the Fermi energy) and the magnetic field applied perpendicularly to the graphene sheet, and characteristic conductance contour patterns are observed at low temperatures. In particular, two types of high-conductance contour lines, i.e., straight and paraboliclike high-conductance contour lines, are found in the measurements. The theoretical calculations are performed within the framework of the tight-binding approach and Green's function formalism. Characteristic high-conductance contour features similar to those in the experiments are found in the calculations. Specifically, the equally spaced, parallel, straight high-conductance contour lines signify the persistence of relativistic quantum scars. The wave functions calculated at points selected along such a straight conductance contour line are found to be dominated by a chain of scars of high-probability distributions arranged as a necklace following the shape of the cavity, and the current density distributions calculated at these point are dominated by an overall vortex in the cavity. These characteristics are found to be insensitive to increasing magnetic field. However, the wave function probability distributions and the current density distributions calculated at points selected along a paraboliclike contour line show a clear dependence on increasing magnetic field, and the current density distributions at these points are characterized by the complex formation of several localized vortices in the cavity. Our work brings insight into quantum chaos in relativistic particle systems and should greatly stimulate experimental and theoretical efforts in this still emerging field.

DOI: [10.1103/PhysRevB.101.085404](https://doi.org/10.1103/PhysRevB.101.085404)**I. INTRODUCTION**

In mesoscopic chaotic structures, the wave functions of eigenstates can coalesce in particular coordinate space to form scars with enhanced probability distributions [1–18]. Typically, the scars are along closed orbits in the semiclassical limit when one considers its classical counterpart, namely, a billiard system where a point particle moves freely inside the billiard and reflects specularly at the boundary [2,3,8]. They can also result from a superposition of several regular eigenstates in a closed structure [4]. It is feasible to measure such quantum scars in an open quantum system via transport measurements. In spite of the fact that coupling to an environment will wash out the characteristics of quantum states, a few eigenstates of the corresponding closed structure, which can effectively mediate the transport, can be selected

and visualized by transport measurements [4,8,19,20]. Scars have been experimentally observed in different systems, including microwave billiard [14,15] and mesoscopic cavities [1,9,16,17,21,22]. For example, at low magnetic fields, certain characteristic patterns in the conductance of an open mesoscopic system are shown to be related to the underlying energy spectrum of the corresponding closed structure [22–24]. But so far, experimental studies of mesoscopic cavities have nearly exclusively been performed in nonrelativistic systems described by the Schrödinger equation with a quadratic energy dispersion in a corresponding infinite system. An interesting question is whether such scars can generally appear with new characteristics in relativistic quantum systems described by the Dirac equation, which, for an infinite system, gives a linear energy dispersion. Graphene is a two-dimensional material consisting of carbon atoms in the honeycomb lattice [25]. Graphene exhibits rich interesting physics properties [26–31], such as linear energy dispersion in the vicinity of the Dirac point, chiral carriers of zero mass, and extremely high mobility. Thus, a graphene cavity is an excellent candidate for the study of quantum scars in a finite relativistic system. Theoretical works have predicted [32–36] unequivocal evidence of

*These authors contributed equally to this work.

†Corresponding author: huangl@lzu.edu.cn

‡Corresponding author: nkang@pku.edu.cn

§Corresponding author: hqxu@pku.edu.cn

quantum scars in relativistic systems, i.e., relativistic quantum scars, which can have a significant effect on the transport properties, such as characteristic conductance fluctuations. On the experimental side, observation of quantum scars was achieved only very recently in a mesoscopic graphene ring device using the scanning gate technique [37]. Nevertheless, direct transport evidence for the existence of relativistic quantum scars has remained elusive.

In this work, we study the transport properties of an open graphene cavity and demonstrate the observation of transport signatures of quantum scars in the relativistic particle system. The cavity is made of chemical vapor deposition (CVD) grown graphene on a substrate of *n*-doped Si covered by a thin layer of SiO₂. The conductance of the graphene cavity is measured as a function of the Fermi energy and magnetic field. Characteristic patterns are found in the measurements and are analyzed in terms of the underlying energy spectra. The system is also studied via theoretical calculations based on the Green's function method. The calculated conductance map (i.e., a plot of the conductance as a function of the Fermi energy and the magnetic field) is found to be in good agreement with the experiment. In both the measured and calculated conductance maps, two distinct types of high-conductance contour lines, i.e., straight and parabolic-like lines, are found. These lines are typically caused by the scar states in the corresponding closed system due to the Fano resonance [38], which are confirmed by the plot of the local density of states (LDOS) and the current density distributions. These lines are inherent in the quantization condition of the scar states and the linear dispersion relation of the graphene cavity, as we shall detail in Sec. III, and thus are the transport signatures of the relativistic quantum scars.

The rest of this paper is organized as follows. Section II explains the experimental details. Section III provides the main results of this work, both experimental and the simulation results with semiclassical analysis, identifying the transport signatures of the underlying scar states. A discussion and conclusions are provided in Sec. IV.

II. EXPERIMENTAL DETAILS

Our graphene cavity device was fabricated on a Si/SiO₂ substrate from monolayer graphene grown via CVD. The fabrication was started by transferring CVD-grown graphene on a substrate of *n*-doped Si covered by a 300-nm-thick layer of SiO₂ [39]. After the transfer, a standard 16- μ m-long and 3- μ m-wide Hall-bar structure with a cavity inside was fabricated by electron beam lithography (EBL) and reactive-ion etching with oxygen plasma. Contacts were subsequently fabricated by an additional step of EBL and deposition of a bilayer of Ti/Au (10 nm/90 nm) by electron beam evaporation. Figure 1(a) displays a false-color atomic force microscope (AFM) image of the fabricated device and a schematic of the measurement setup. The highlighted dark red region is the graphene current channel. The small green regions are graphene flakes which are isolated by narrow trenches from the cavity structure. A zoom-in look at the cavity structure is shown in Fig. 1(b). The graphene cavity structure has an octagonal shape ~ 1 μ m in size and is connected to bulk graphene via two 400-nm-wide constrictions. The device also

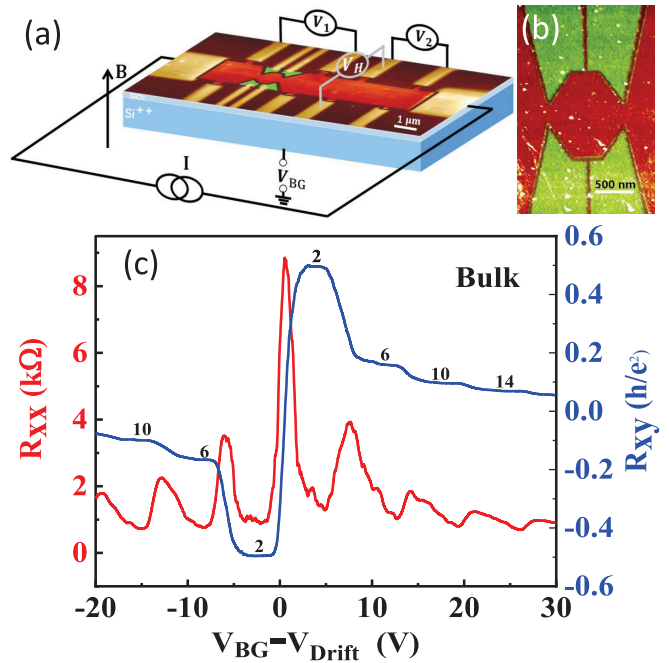


FIG. 1. Graphene cavity structure. (a) False-colored atomic force microscope (AFM) image of the graphene device and schematics for the device structure and measurement setup. Yellow parts are electrodes. The red region is graphene. Green highlighted regions are graphene pieces isolated from the cavity by etched trenches, which could be used as side gates but are not used in this work. The device is made on a Si/SiO₂ substrate which is used as a back gate. *V*₁ and *V*₂ denote the voltage drops over the cavity and a graphene bulk region, respectively, and *V*_H is the Hall voltage generated in the graphene bulk region. (b) Zoom-in AFM image of the cavity structure in (a). (c) Hall resistance *R*_{xy} and longitudinal resistance *R*_{xx} of the graphene bulk region measured at perpendicularly applied magnetic field *B* = 5 T and temperature *T* = 60 mK. *V*_{BG} is the applied back gate voltage, and *V*_{Drift} is the drifting gate voltage of the Dirac point.

consists of a region without a fine cavity structure. This arrangement enables us to directly compare the transport measurements of the cavity structure with bulk graphene on the same device. The measurements were carried out by applying a constant current *I* through the two most distant contacts, that is, the source and the drain, and recording voltage drop *V*₁ over the cavity structure and voltage drop *V*₂ over the graphene bulk at the same time. The conductance of the cavity region is obtained as *G*₁ = *I*/*V*₁, and the conductance of the reference bulk region is obtained as *G*₂ = *I*/*V*₂. The magnetotransport measurements were performed in a ³He/⁴He dilution refrigerator with magnetic field *B* applied perpendicular to the graphene plane, using a standard ac lock-in technique (with a current bias of 10–100 nA at a frequency of 13 Hz).

III. RESULTS AND DISCUSSION

A. Graphene bulk character

Before comparative studies of the cavity with the graphene bulk, the graphene sheet was characterized by standard Hall measurements. Figure 1(c) shows the measured Hall resistance *R*_{xy} and longitudinal resistance *R*_{xx} in the bulk graphene

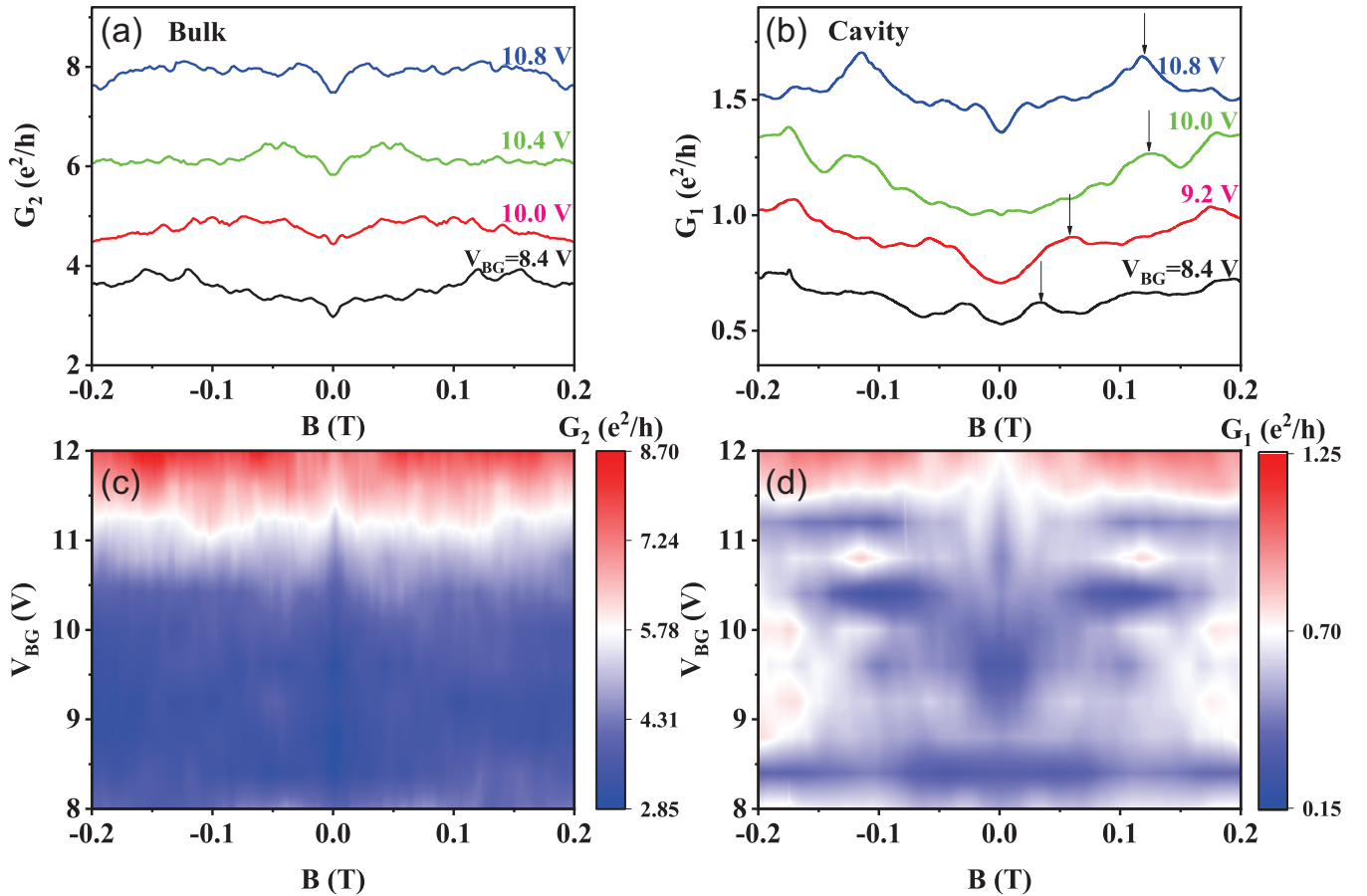


FIG. 2. Low-temperature magnetotransport in the graphene cavity structure. (a) Longitudinal conductance of the graphene bulk region measured as a function of the magnetic field B at different back gate voltages V_{BG} and temperature $T = 60$ mK. Curves are successively vertically offset by $1e^2/h$ for clarity. (b) Conductance of the graphene cavity measured as a function of B at different back gate voltages V_{BG} and temperature $T = 60$ mK. Curves are successively vertically offset by $0.15e^2/h$. Black arrows denote the positions of conductance peaks which evolve with increasing back gate voltage. (c) Conductance map of the bulk graphene region, i.e., longitudinal conductance measured for the bulk graphene region as a function of V_{BG} and B at $T = 60$ mK. (d) Conductance map of the graphene cavity at $T = 60$ mK.

region at magnetic field $B = 5$ T at 60 mK. Here, well-developed quantized Hall plateaus are observed, demonstrating the high quality of the graphene [26]. The mobility extracted from the measurements is around $17\,000\text{ cm}^2\text{ V}^{-1}\text{ s}^{-1}$ at carrier density $n \approx 1.0 \times 10^{11}\text{ cm}^{-2}$, and the mean free path l_e derived from semiclassical relation [31] $l_e = (\hbar/e)\mu(\pi n)^{1/2}$ is about 100 nm. This indicates the existence of scatterers in the phase-coherent transport, but our results are robust, as shown by the numerical simulations with the same number of scatterers as in the experiment (see Supplemental Material, Figs. S6 and S7 [40]).

B. Conductance map of the graphene cavity and bulk

Figures 2(a) and 2(b) show the conductance G_2 of the bulk graphene region and the conductance G_1 of the cavity region measured as a function of the magnetic field at different back gate voltages. Here and in the following, the longitudinal bulk graphene conductance is denoted by G_2 . In Fig. 2(a), the features of universal conductance fluctuations (UCFs) [41], i.e., aperiodic fluctuations with fluctuation amplitude $\delta g_{2D} \approx 0.2e^2/h$, are observable. Through the theoretical prediction

[41] of $\delta g_{2D} \approx L_\phi(W^{1/2}/L^{3/2})\delta g_0$, where W and L are the width and the length of the bulk graphene Hall bar, L_ϕ is the phase coherence length, and $\delta g_0 \sim e^2/h$, the phase coherence length in our graphene sample is estimated to be on the order of $1\text{ }\mu\text{m}$, which is consistent with previous experiments [42]. In Fig. 2(b), instead of showing UCFs, the conductance curves are smoother. In addition, we can observe that conductance peaks (indicated by black arrows) appear at some particular magnetic fields. These characteristics remind us about the conductance enhancements via transport through the eigenstates of the corresponding closed system [4]. To explore the evolution of these conductance peaks further, we performed the conductance map measurements, i.e., the measurements of the conductance as a function of the back gate voltage and the magnetic field, for both the bulk and cavity regions. Figures 2(c) and 2(d) show the measured conductance maps (on a color scale) for the bulk and cavity regions in a back gate voltage window of $V_{BG} = 8$ to 12 V and a magnetic field window of -0.2 to 0.2 T. The red regions in Fig. 2(c) and 2(d) represent the regions with high conductance. It is seen in Fig. 2(d) that the measured conductance map exhibits a characteristic “monkey face” pattern of enhanced conductance. However,

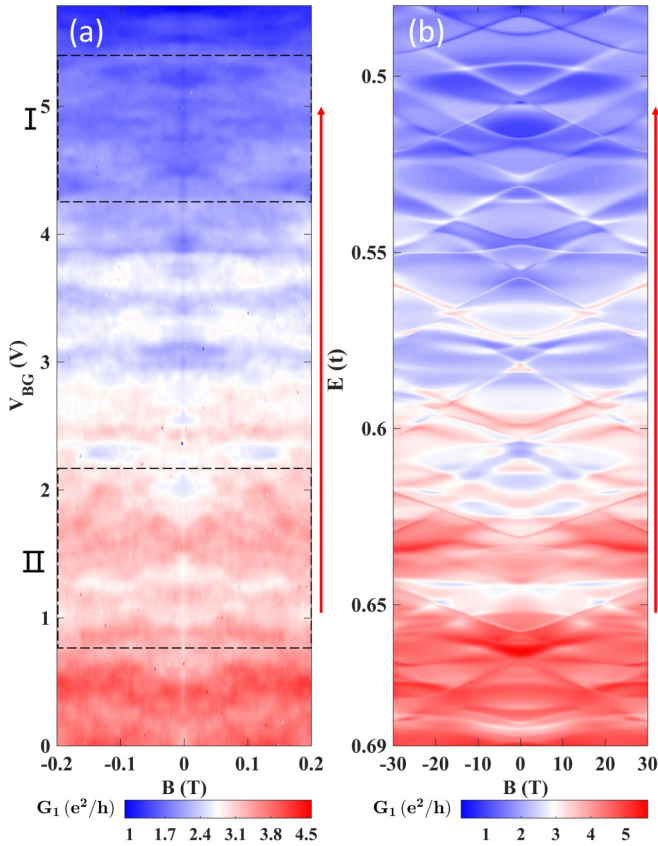


FIG. 3. Characteristic conductance patterns. (a) Conductance map of the graphene cavity measured at temperature $T = 60$ mK over a large range of V_{BG} . (b) Simulated conductance map of the graphene cavity. Here, similar characteristic conductance patterns are found in the measurements and the calculations. The red arrows point to the direction towards the Dirac point.

the measured conductance map shown in Fig. 2(c) displays a nearly structureless distribution of the conductance. In early experiments, characteristic features similar to those seen in Fig. 2(d) were found and were linked to the underlying energy spectra of closed quantum cavities [4,22–24,43]. Furthermore, because the carriers injected through a quantum point contact will be in a collimated form [3,5,22,44–47], carriers can enter the cavity with a sufficiently large probability only at certain angles, and thus, only some particular eigenstates can be preferentially excited and can contribute to the carrier transport.

C. Conductance map and theoretical simulations of the graphene cavity

Figure 3(a) is the conductance map measured in the same magnetic field window of -0.2 to 0.2 T but a back gate voltage window of $V_{BG} = 0$ to 5.8 V. The Dirac point is around $V_{Dirac} \approx 9$ V [48]. Red arrows beside the graph indicate the direction towards the Dirac point. Here, as we expected, the overall conductance is found to decrease with increasing back gate voltage, i.e., when the Fermi level moves towards the Dirac point. But, more importantly, the measured conductance map is found to exhibit complex contour patterns. To better

understand these complex features, full quantum-mechanical transport calculations were performed for the graphene cavity structure within the Landauer formalism [49], which relates the zero-temperature two-terminal conductance G of the device to the transmission coefficient T in the form of $G = \frac{2e^2}{h}T$. The transmission coefficient T was calculated in the Green's function scheme within the tight-binding framework [32,34,50,51]. The tight-binding Hamiltonian for electrons in graphene including the hopping terms up to the third-nearest-neighbor atoms takes the form [52–54],

$$\hat{H} = -t \sum_{i,j \in \text{n.n.}} e^{-i\phi_{ij}} c_i^\dagger c_j - t' \sum_{i,j \in \text{n.n.n.}} e^{-i\phi_{ij}} c_i^\dagger c_j - t'' \times \sum_{i,j \in \text{t.n.n.}} e^{-i\phi_{ij}} c_i^\dagger c_j, \quad (1)$$

where t , t' , t'' represent the nearest-neighbor (n.n.), next-nearest-neighbor (n.n.n.), and third-nearest-neighbor (t.n.n.) hopping energies, which take the values of 2.8, 0.28, and 0.07 eV [52–54], respectively, and $\phi_{ij} = (2\pi/\phi_0) \int_{\mathbf{r}_j}^{\mathbf{r}_i} d\mathbf{r} \cdot \mathbf{A}$, where $\phi_0 = h/e$ is the magnetic flux quantum and \mathbf{A} is the vector potential associated with the applied magnetic field. Using the Landau gauge, the vector potential is given by $\mathbf{A} = (By, 0, 0)$ for a perpendicular uniform magnetic field \mathbf{B} pointing out of the cavity plane. The magnetic field is applied only in the device region in our simulation. Note that the Dirac point will be shifted to $3t'$ when considering the next-nearest-neighbor hopping energy [52]. Close to the Dirac point, the pseudoparticles in graphene are described by the Dirac Hamiltonian, $\hat{H} = v_F \hat{\sigma} \cdot \hat{\mathbf{p}} + U(\mathbf{r})$ with the spinor wave function $\Psi = [\Psi_1, \Psi_2]^T$, where v_F is the Fermi velocity, $\hat{\sigma}$ are the Pauli matrices, $U(\mathbf{r})$ is the confinement or disorder potential, and the pseudospin is actually the relative wave function distribution on the two nonequivalent carbon atoms. Transport properties can be calculated using the Dirac Hamiltonian [55,56], while here we would constrain ourselves by solving the tight-binding Hamiltonian (1).

The cavity device can be split into three parts: left lead, cavity, and right lead. The two leads are assumed to be semi-infinite to simulate the open boundaries [41]. The Green's function of the device is given by $G_D(E) = (EI - H_D - \Sigma_L - \Sigma_R)^{-1}$, where Σ_L and Σ_R are the self-energies caused by the left and right leads and H_D is the tight-binding Hamiltonian of the graphene cavity with hopping terms up to the third-nearest-neighbor atoms included. The coupling matrices between the leads and the cavity, $\Gamma_L(E)$ and $\Gamma_R(E)$, are given in terms of self-energies $\Gamma_{L,R} = i(\Sigma_{L,R} - \Sigma_{L,R}^\dagger)$. The transmission T is given by $T(E) = \text{Tr}(\Gamma_L G_D \Gamma_R G_D^\dagger)$. The LDOS can be obtained by $\rho = -\frac{1}{\pi} \text{Im}[\text{diag}(G_D)]$. The local current flow is given by $J_{i \rightarrow j} = \frac{4e}{h} \text{Im}[H_{D,ij} C_{ji}^n(E)]$ [41], where $C^n = G_D \Gamma^L G_D^\dagger$ is the electron correlation function. The graphene cavity for the simulation is scaled down from the experimental one to a size of 19.2 by 16 nm², i.e., between the upper and lower boundaries and between the two narrow constrictions.

Figure 3(b) shows the results of the calculations, which clearly succeed in reproducing the main features of the experimental results shown in Fig. 3(a). The satisfactory agreement between the experiment and the theory inspires us to get further understanding of the characteristic patterns of

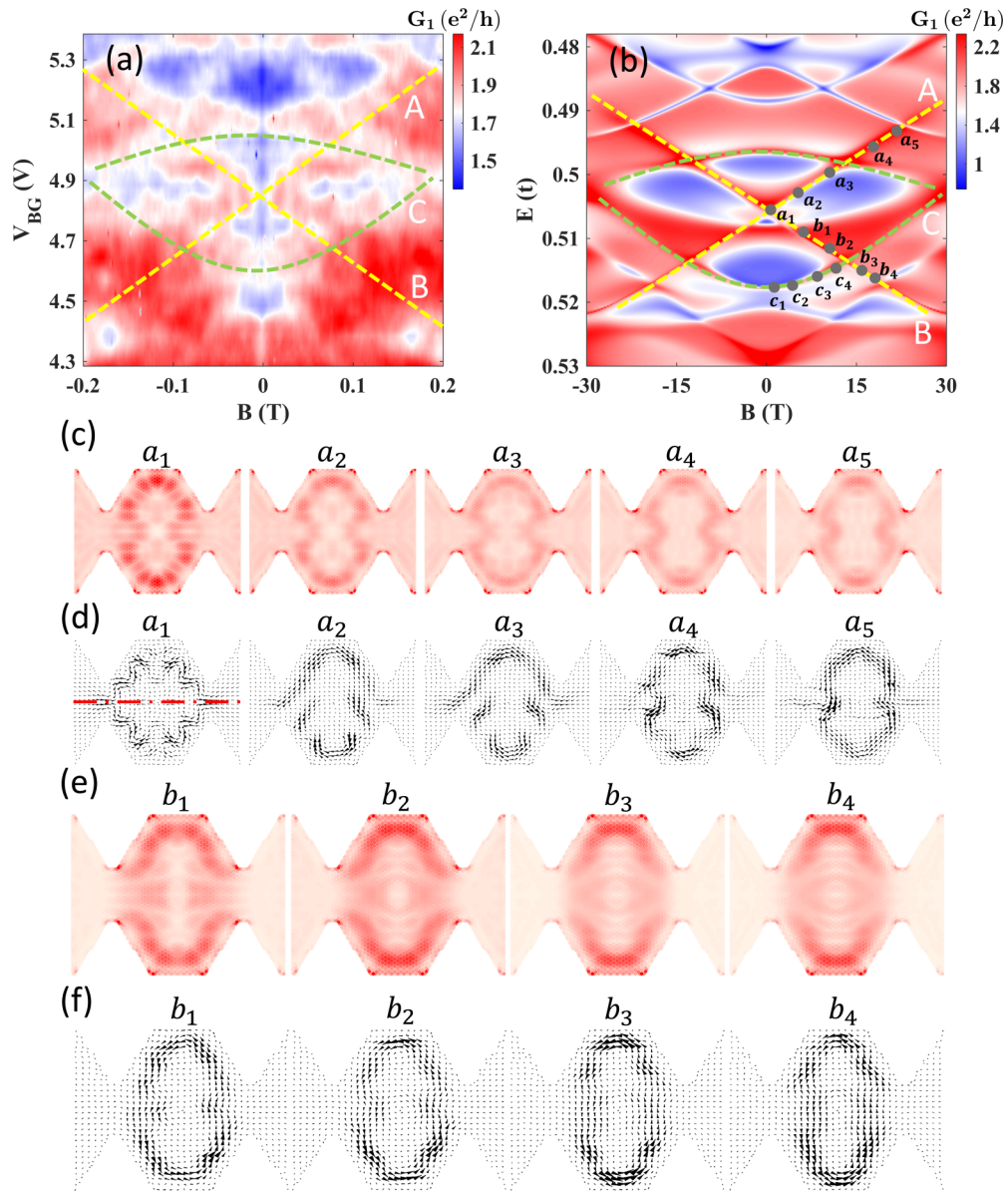


FIG. 4. Conductance patterns in region I near the Dirac point. (a) and (b) Zoom-in plot of the measurements shown in rectangular region I of Fig. 3(a) and zoom-in plot of the calculations in the corresponding region shown in Fig. 3(b). Straight (paraboliclike) high-conductance contour lines are highlighted with yellow (green) dashed lines. (c) and (d) Calculated wave function probability distributions and current density distributions at points a_n , where $n = 1, 2, 3, 4$, and 5, selected along straight line A. Here, it is seen that the scar pattern does not show a significant change with increasing magnetic field, and the current density distribution in each panel shows only one clockwise current vortex. (e) and (f) Calculated wave function probability distributions and current density distributions at points b_m , where $m = 1, 2, 3$, and 4, selected along straight contour line B. Characteristic features in the wave function probability distributions and the current density distributions similar to those in (c) and (d) are observed, except that the current vortex seen in each current density distribution is counterclockwise.

high-conductance contour lines by making a close comparison between Figs. 3(a) and 3(b). Let us focus on the regions marked by the two dashed rectangles in Fig. 3(a), which we label as regions I and II. We note that region I is closer to the Dirac point than region II.

D. The LDOS and current density distribution along high-conductance contour lines

Figure 4(a) is a close-up plot of the measurements in region I in Fig. 3(a), while Fig. 4(b) is a close-up plot of the calcu-

lations in the corresponding region shown in Fig. 3(b). Here more featured high-conductance contour lines are observable. Surprisingly, the patterns observed in the measurements and the calculations are still well matched. Both Figs. 4(a) and 4(b) show similar straight high-conductance contour lines (see, e.g., the lines marked by yellow dashed lines A and B) and paraboliclike high-contour lines (see, e.g., the lines marked by green dashed lines C). To get physical insight into these characteristic high-conductance contour lines, we have computed the LDOS and the current density distribution at a few selected points in the (B, E) parameter plane along

the lines. In the tight-binding formulation (see Supplemental Material, Eqs. (11) and (12) [40]), the LDOS provides the wave function probability spatial distribution (or charge density spatial distribution) contributed by all the states at energy E and a given magnetic field B , while the current density spatial distribution provides information about current paths for carriers with energy E to pass through the cavity at magnetic field B .

Figures 4(c) and 4(d) show the calculated LDOS and current density distribution at five selected points, denoted by a_n , with $n = 1, 2, 3, 4$, and 5, along straight high-conductance contour line A in Fig. 4(b). Red regions in Fig. 4(c) correspond to the regions with high charge density probability distributions. Note that here the color scales in different panels are different. The patterns seen in Fig. 4(c) are highly reminiscent of scars of enhanced wave function probabilities in coordinate space [4,11]. For example, at point a_1 , the wave functions are highly localized to the regions close to the boundary of the cavity, looking like a chain of pearls (scars) arranged in a peanut-shell-like structure. At point a_2 , where a finite magnetic field is applied, the wave functions remain localized to the regions close to the boundary of the cavity. The same localization characteristics are also seen in the wave function probability distributions at points a_3 to a_5 , although the scars become slightly smeared. In Fig. 4(d), the corresponding current density distributions calculated at the same five selected points along straight high-conductance contour line A are plotted. Here it is seen that at zero magnetic field, i.e., at point a_1 , the current density distribution is symmetric with respect to the horizontal axis (marked by a dot-dashed red line). On both the upper and lower sides of the axis, we see an overall current flow from the left to the right, although several sharp current turns inside the cavity are observable. At finite magnetic fields, i.e., at points a_2 to a_5 , the current density distributions are no longer symmetric with respect to the horizontal axis. Here on the upper side the current flows from the left to the right, while on the lower side the current flows from the right to the left, leading to the formation of an overall clockwise current vortex in the cavity. Note that here a net current passing through the cavity still continues to flow from the left to the right. Note also that although we find that the wave function probability distribution patterns at points a_2 to a_5 are very similar in Fig. 4(c), their corresponding current density distributions shown in Fig. 4(d) do exhibit small, but noticeable differences. For example, although very similar current density distribution patterns are found at points a_2 and a_3 and at points a_4 and a_5 , a small difference can be seen when the current density distribution patterns at points a_3 and a_4 are compared. This difference is most likely caused by the difference in mixing of the scar states with other states since the two points lie on the two sides of another high-conductance contour line.

Similar localization characteristics have been found in the calculated wave function probability distributions and current density distributions at points b_m , with $m = 1, 2, 3$, and 4, selected along high-conductance contour line B. Here the wave functions [Fig. 4(e)] are again highly localized to form a chain of scars in the regions close to the boundary of the cavity, and the current density distributions [Fig. 4(f)] are seen to form an overall vortex in the cavity. However, it is

interesting to note that the current vortex found at each of these points rotates counterclockwise, in contrast to the results obtained at points a_2 to a_5 . This difference is consistent with the fact that high-conductance contour line B has a negative slope, which is in contrast to line A (line A has a positive slope).

Therefore, the high-conductance contour lines are typically associated with localized scar states, or pointer states [7], due to the Fano resonance [38]. The occurrence of the scar states satisfies the semiclassical quantization condition, which yields the position in the parameter space (B, E) where a given scar state can form and, consequently, where a conductance peak may occur. Thus, the relation between B and E from the quantization condition, which forms the energy spectrum of the corresponding closed system, yields the high-conductance contour lines in the conductance map. Note that only localized scar states that have fewer interactions with the leads can survive as the system is opened [7,22]. In particular, along a high-conductance contour line for a graphene cavity, the energy of the state in the cavity is approximately proportional to the magnetic flux penetrating through an effective area S enclosed in the current paths of an effective total length L , i.e., $E = E_0 \pm (v_F e S / L) B$ [36], where the sign depends on the orientation of the local current circulating the magnetic flux. As we showed above, with increasing magnetic field along a straight high-conductance contour line, the wave function probability distributions and the current density distributions remain roughly the same. Thus, the effective area enclosed in the current vortex is approximately unchanged with increasing magnetic field. As a result, the energy of the states increases linearly with increasing magnetic field, as seen in line A in Figs. 4(a) and 4(b). Following the quantization rule, the scar state will recur when we vary the Fermi energy or magnetic fields; for example, when B is fixed, $\Delta E = h v_F / L$ [33]. A unique feature of the relativistic case is that, for the same scar state with fixed S and L , the slope of the straight high-conductance contour lines, dE/dB , will be the same, i.e., $v_F e S / L$. This leads to the equally spaced, parallel, straight high-conductance contour lines in the conductance map in the (B, E) parameter space, as shown in Fig. 3(b), which signifies the presence of the relativistic quantum scars. The negative slope seen in line B is because here the current vortices are counterclockwise and thus the magnetic flux penetrating the effective area enclosed in each of these vortices carries an opposite sign. However, for the nonrelativistic case, in contrast, the general functional form between E and B is parabolic, but off-center, with the minimum point shifted away from $B = 0$. However, when the scale is small, e.g., for $B \sim 0$, it can still be approximated by a straight line, but on one side, these lines are not equally spaced; they become sparser as the energy goes higher. On the other side, the slope dE/dB will not be a constant as it varies with both the energy and the magnetic field, and for $B = 0$, $dE/dB \propto \sqrt{E_{B=0}}$, where $E_{B=0}$ is the corresponding energy of the cross point of the high-conductance contour line with the E axis. Thus, as the energy becomes larger, these lines become sparser, and in the meantime, the slope increases (see the Supplemental Material, Fig. S4(b) [40]), in strong contrast to the equally spaced, parallel, straight high-conductance contour lines in the conductance map.

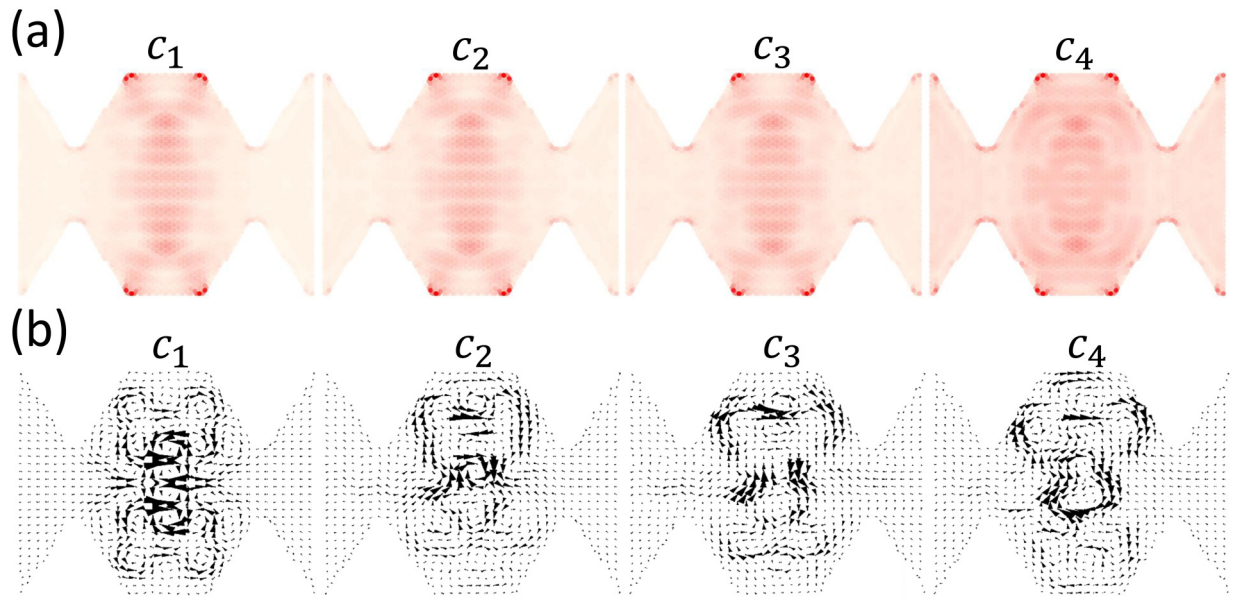


FIG. 5. (a) and (b) Calculated wave function probability distributions and current density distributions at points c_k , where $k = 1, 2, 3,$ and 4 , selected along paraboliclike contour line C in Fig. 4(b). Here, the scar distribution pattern shows change sensitive to change in magnetic field, and the current density distribution exhibits the formation of a complex structure consisting of several localized clockwise and counterclockwise current vortices.

Figures 5(a) and 5(b) show the calculated LDOS and current density distributions at selected points c_k , with $k = 1, 2, 3,$ and 4 , along paraboliclike high-conductance contour line C shown in Fig. 4(b). Again, the charge density distributions shown in Fig. 5(a) are all symmetric with respect to the horizontal axis. But such symmetry is found in the current density distribution only at zero magnetic field, as seen in panel c_1 of Fig. 5(b). However, when comparing these results to the results shown in Figs. 4(c) to 4(f), significant differences are found. First, high-density spots localized in the middle of the cavity and arranged as vertically elongated X patterns are found in the charge density distributions. Thus, no closed orbitlike structures are seen. Second, much more complex structures are seen in the current density distributions. In particular, several small current vortices are present in the current density distributions and are spread over the cavity. Third, at zero magnetic field, clockwise- and counterclockwise-orientated current vortices are symmetrically localized in the cavity, and the areas enclosed by all clockwise- and all counterclockwise-orientated vortices are equal. But with increasing magnetic field, the area enclosed by all vortices oriented in one direction (say, clockwise) grows slowly, and the area enclosed by all vortices oriented in the opposite direction (say, counterclockwise) shrinks. This difference in the area enclosed by the vortices in two different directions at finite magnetic field is in contrast to the results shown in Figs. 4(d) and 4(f); that is, instead of being a constant, the effective circulating area S in this case increases with increasing magnetic field, which could be the origin of the observed paraboliclike magnetic field dependence of the energy as revealed by the high-conductance contour lines C shown in Figs. 4(a) and 4(b).

Figure 6(a) shows a close-up plot of the measured conductance map in region II in Fig. 3(a), and Fig. 6(b) shows a plot of the calculated conductance map in the corresponding

region. By comparison of the results shown in Figs. 6(a) and 6(b), similar features can again be found in the measurements and calculations. Straight high-conductance contour lines can be recognized and are marked by dashed yellow lines. Figures 6(c) and 6(d) show the calculated LDOS and the current density distributions at four selected points d_l , with $l = 1, 2, 3,$ and 4 , along yellow dashed line D in Fig. 6(b). Here, as we have seen in Figs. 4(c) to 4(f), the charge density distributions and the current density distributions shown in Figs. 6(c) and 6(d) display similar ringlike orbit structures and exhibit little changes with increasing magnetic field. This result is consistent with the linear dependence of the state energy on the magnetic field, as we discussed above. However, comparing these results to the results calculated for region I in Fig. 4, here we can recognize clearly that additional current paths appear along the edges of the cavity. This might manifest the higher conductance observed in this region far from the Dirac point.

IV. CONCLUSION

In summary, we have studied the quantum transport properties of a relativistic quantum cavity. The cavity was made from a CVD-grown graphene sheet on a Si/SiO₂ substrate. Low-temperature measurements of the conductance map, i.e., the conductance in the linear response regime as a function of the back gate voltage and the magnetic field applied perpendicular to the graphene plane, have been carried out for the cavity device. The complex characteristic features were found in the measured conductance map. To analyze the underlying physics revealed in these measurements, the graphene cavity device was modeled by a third-nearest-neighbor tight-binding Hamiltonian, and the conductance, charge density distribution, and current density distribution were calculated

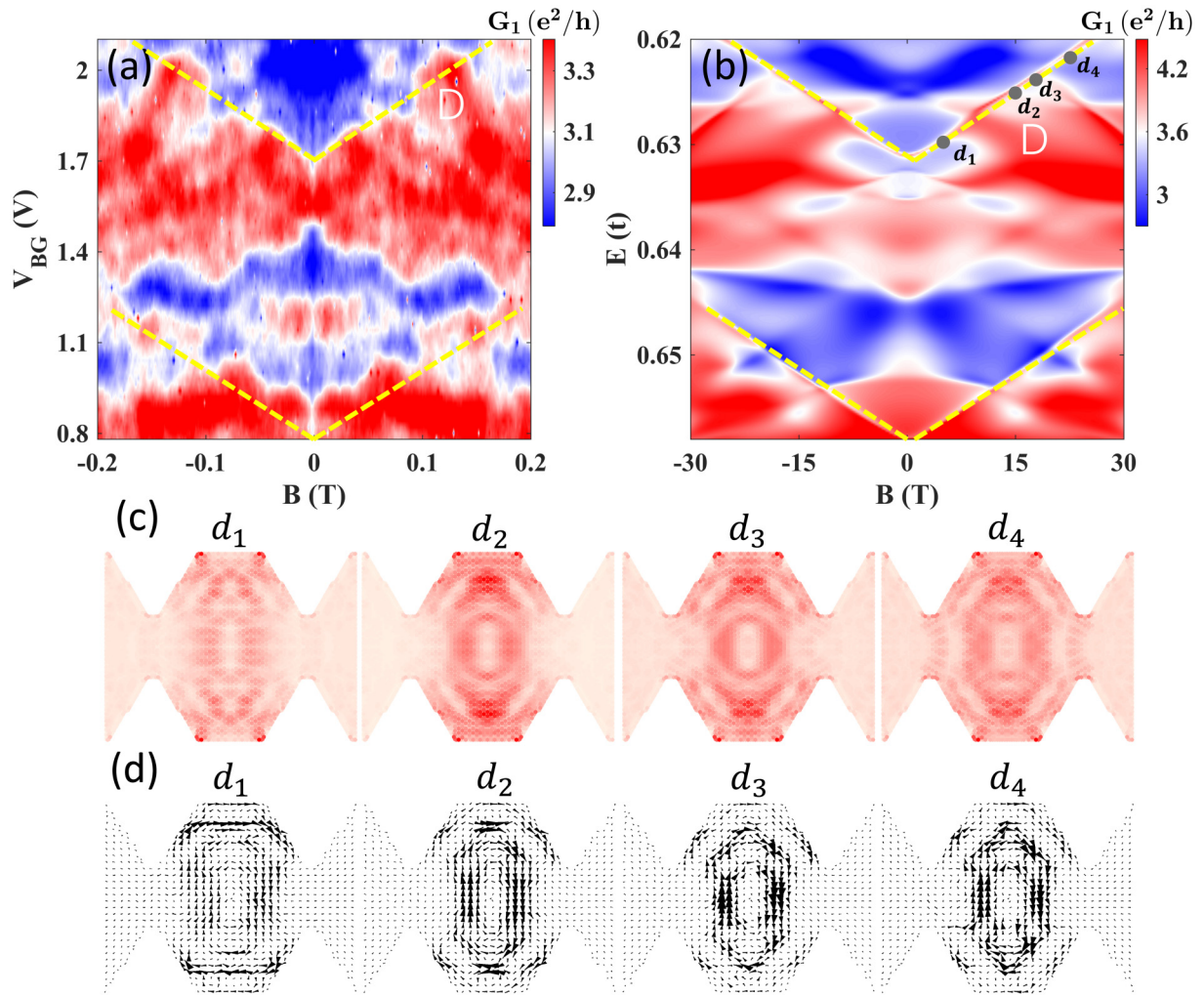


FIG. 6. Conductance patterns in region II. (a) and (b) Zoom-in plot of the measurements shown in rectangular region II in Fig. 3(a) and zoom-in plot of the calculations in the corresponding region shown in Fig. 3(b). Note that region II is far from the Dirac point compared with region I. Yellow dashed lines highlight straight high-conductance contour lines observable in the measurements and the calculations. (c) and (d) Calculated wave function probability distributions and current density distributions at points d_l , where $l = 1, 2, 3,$ and 4 , selected along straight line D in (b). Characteristic features in the charge density distributions and the current density distributions similar to those in Fig. 4 are observed, except that a well-defined additional current path along the edge of the cavity is observable in each current density distribution panel.

based on the Green's function formalism. The calculated conductance map exhibits complex characteristics similar to those observed in the measurements. The calculated charge density distributions show the formation of scars, and the current density distributions display the formation of complex vortices in the cavity. In particular, both straight and paraboliclike high-conductance contour lines were found in the calculated and measured conductance maps. It has been found that along a straight high-conductance contour line, the scar pattern remains almost unchanged with increasing magnetic field, while the circulating direction of the current in the cavity at finite magnetic field is closely related to the slope of the contour line: it circulates clockwise when the contour line has a positive slope but counterclockwise when the contour line has a negative slope. It should be emphasized that the equally spaced, parallel, straight high-conductance contour lines and the associated characteristics found in the

scar pattern and the current density distribution are inherit in a relativistic quantum cavity. However, along a paraboliclike high-conductance contour line, it has been found that the charge density distribution displays a complex scar pattern and the current density distribution exhibits the formation of several local vortices. Furthermore, although at zero magnetic field the total effective areas enclosed by the vortices circulating in opposite directions are the same, this balance is broken at a finite magnetic field, and the difference in the total effective area enclosed by the vortices of opposite directions changes with increasing magnetic field. A paraboliclike high-conductance contour line has been commonly observed for a nonrelativistic quantum system at low Fermi energy. Here we showed it can also be observed in a relativistic quantum cavity but with a completely different mechanism. We expect that our work will stimulate experimental and theoretical studies of quantum chaos in relativistic quantum systems.

ACKNOWLEDGMENTS

We acknowledge financial support from the Ministry of Science and Technology of China (MOST) through the National Key Research and Development Program of China (Grants No. 2016YFA0300601 and No. 2017YFA0303304),

the National Natural Science Foundation of China (Grants No. 11874071, No. 11774005, No. 11974026, and No. 11775101), and the Beijing Academy of Quantum Information Sciences (Grant No. Y18G22).

-
- [1] J. P. Bird, K. Ishibashi, Y. Aoyagi, T. Sugano, R. Akis, D. K. Ferry, D. P. Pivin, Jr, K. M. Connolly, R. P. Taylor, R. Newbury, D. M. Olatona, A. Micolich, R. Wirtz, Y. Ochiai, and Y. Okubo, Quantum transport in open mesoscopic cavities, *Chaos, Solitons Fractals* **8**, 1299 (1997).
- [2] J. P. Bird, D. K. Ferry, R. Akis, Y. Ochiai, K. Ishibashi, Y. Aoyagi, and T. Sugano, Periodic conductance fluctuations and stable orbits in mesoscopic semiconductor billiards, *Europhys. Lett.* **35**, 529 (1996).
- [3] R. Akis, D. K. Ferry, and J. P. Bird, Magnetotransport fluctuations in regular semiconductor ballistic quantum dots, *Phys. Rev. B* **54**, 17705 (1996).
- [4] I. V. Zozoulenko and K.-F. Berggren, Quantum scattering, resonant states, and conductance fluctuations in an open square electron billiard, *Phys. Rev. B* **56**, 6931 (1997).
- [5] J. P. Bird, R. Akis, D. K. Ferry, Y. Aoyagi, and T. Sugano, Periodic conductance fluctuations and lead-induced scarring in open quantum dots, *J. Phys.: Condens. Matter* **9**, 5935 (1997).
- [6] D. K. Ferry, R. A. Akis, D. P. Pivin, Jr, J. P. Bird, N. Holmberg, F. Badrieh, and D. Vasileska, Quantum transport in ballistic quantum dots, *Phys. E (Amsterdam, Neth.)* **3**, 137 (1998).
- [7] D. K. Ferry, R. Akis, and J. P. Bird, Einselection in Action: Decoherence and Pointer States in Open Quantum Dots, *Phys. Rev. Lett.* **93**, 026803 (2004).
- [8] D. K. Ferry, R. Akis, and J. P. Bird, Einselection and the quantum to classical transition in quantum dots, *J. Phys.: Condens. Matter* **17**, S1017 (2005).
- [9] R. Akis, D. K. Ferry, and J. P. Bird, Wave Function Scarring Effects in Open Stadium Shaped Quantum Dots, *Phys. Rev. Lett.* **79**, 123 (1997).
- [10] R. Akis, J. P. Bird, and D. K. Ferry, The persistence of eigenstates in open quantum dots, *Appl. Phys. Lett.* **81**, 129 (2002).
- [11] E. J. Heller, Bound-State Eigenfunctions of Classically Chaotic Hamiltonian Systems: Scars of Periodic Orbits, *Phys. Rev. Lett.* **53**, 1515 (1984).
- [12] E. B. Bogomolny, Smoothed wave functions of chaotic quantum systems, *Phys. D (Amsterdam, Neth.)* **31**, 169 (1988).
- [13] M. V. Berry, Quantum scars of classical closed orbits in phase space, *Proc. R. Soc. London, Ser. A* **423**, 219 (1989).
- [14] S. Sridhar, Experimental Observation of Scarred Eigenfunctions of Chaotic Microwave Cavities, *Phys. Rev. Lett.* **67**, 785 (1991).
- [15] J. Stein and H.-J. Stöckmann, Experimental Determination of Billiard Wave Functions, *Phys. Rev. Lett.* **68**, 2867 (1992).
- [16] C. M. Marcus, A. J. Rimberg, R. M. Westervelt, P. F. Hopkins, and A. C. Gossard, Conductance Fluctuations and Chaotic Scattering in Ballistic Microstructures, *Phys. Rev. Lett.* **69**, 506 (1992).
- [17] T. M. Fromhold, P. B. Wilkinson, F. W. Sheard, L. Eaves, J. Miao, and G. Edwards, Manifestations of Classical Chaos in the Energy Level Spectrum of a Quantum Well, *Phys. Rev. Lett.* **75**, 1142 (1995).
- [18] H.-Y. Xu, L. Huang, Y.-C. Lai, and C. Grebogi, Chiral Scars in Chaotic Dirac Fermion Systems, *Phys. Rev. Lett.* **110**, 064102 (2013).
- [19] W. H. Zurek, Environment-induced superselection rules, *Phys. Rev. D* **26**, 1862 (1982).
- [20] W. H. Zurek, Decoherence, einselection, and the quantum origins of the classical, *Rev. Mod. Phys.* **75**, 715 (2003).
- [21] J. P. Bird, D. M. Olatona, R. Newbury, R. P. Taylor, K. Ishibashi, M. Stopa, Y. Aoyagi, T. Sugano, and Y. Ochiai, Lead-induced transition to chaos in ballistic mesoscopic billiards, *Phys. Rev. B* **52**, R14336 (1995).
- [22] R. Akis, D. K. Ferry, J. P. Bird, and D. Vasileska, Weak localization in ballistic quantum dots, *Phys. Rev. B* **60**, 2680 (1999).
- [23] M. Persson, J. Pettersson, B. von Sydow, P. E. Lindelof, A. Kristensen, and K. F. Berggren, Conductance oscillations related to the eigenenergy spectrum of a quantum dot in weak magnetic fields, *Phys. Rev. B* **52**, 8921 (1995).
- [24] I. V. Zozoulenko, A. S. Sachrajda, C. Gould, K.-F. Berggren, P. Zawadzki, Y. Feng, and Z. Wasilewski, Few-Electron Open Dots: Single Level Transport, *Phys. Rev. Lett.* **83**, 1838 (1999).
- [25] K. S. Novoselov, A. K. Geim, S. V. Morozov, D. Jiang, Y. Zhang, S. V. Dubonos, I. V. Grigorieva, and A. A. Firsov, Electric field effect in atomically thin carbon films, *Science* **306**, 666 (2004).
- [26] Y. Zhang, Y.-W. Tan, H. L. Stormer, and P. Kim, Experimental observation of the quantum Hall effect and berry's phase in graphene, *Nature (London)* **438**, 201 (2005).
- [27] L. Yang, M. L. Cohen, and S. G. Louie, Excitonic effects in the optical spectra of graphene nanoribbons, *Nano Lett.* **7**, 3112 (2007).
- [28] E. McCann, K. Kechedzhi, V. I. Fal'ko, H. Suzuura, T. Ando, and B. L. Altshuler, Weak-localization Magnetoresistance and Valley Symmetry in Graphene, *Phys. Rev. Lett.* **97**, 146805 (2006).
- [29] C. Chen, S. Rosenblatt, K. I. Bolotin, W. Kalb, P. Kim, I. Kymissis, H. L. Stormer, T. F. Heinz, and J. Hone, Performance of monolayer graphene nanomechanical resonators with electrical readout, *Nat. Nanotechnol.* **4**, 861 (2009).
- [30] A. H. Castro Neto, F. Guinea, N. M. R. Peres, K. S. Novoselov, and A. K. Geim, The electronic properties of graphene, *Rev. Mod. Phys.* **81**, 109 (2009).
- [31] K. I. Bolotin, K. J. Sikes, Z. Jiang, M. Klima, G. Fudenberg, J. Hone, P. Kim, and H. L. Stormer, Ultrahigh electron mobility in suspended graphene, *Solid State Commun.* **146**, 351 (2008).
- [32] L. Huang, Y.-C. Lai, D. K. Ferry, R. Akis, and S. M. Goodnick, Transmission and scarring in graphene quantum dots, *J. Phys.: Condens. Matter* **21**, 344203 (2009).

- [33] L. Huang, Y.-C. Lai, D. K. Ferry, S. M. Goodnick, and R. Akis, Relativistic Quantum Scars, *Phys. Rev. Lett.* **103**, 054101 (2009).
- [34] D. K. Ferry, L. Huang, R. Yang, Y.-C. Lai, and R. Akis, Open quantum dots in graphene: Scaling relativistic pointer states, *J. Phys.: Conf. Ser.* **220**, 012015 (2010).
- [35] L. Huang, Y.-C. Lai, and C. Grebogi, Characteristics of level-spacing statistics in chaotic graphene billiards, *Chaos* **21**, 013102 (2011).
- [36] L. Ying, L. Huang, Y.-C. Lai, and C. Grebogi, Conductance fluctuations in graphene systems: The relevance of classical dynamics, *Phys. Rev. B* **85**, 245448 (2012).
- [37] D. Cabosart, A. Felten, N. Reckinger, A. Iordanescu, S. Toussaint, S. Faniel, and B. Hackens, Recurrent quantum scars in a mesoscopic graphene ring, *Nano Lett.* **17**, 1344 (2017).
- [38] L. Huang, Y.-C. Lai, H.-G. Luo, and C. Grebogi, Universal formalism of fano resonance, *AIP Adv.* **5**, 017137 (2015).
- [39] L. Lin, J. Li, H. Ren, A. L. Koh, N. Kang, H. Peng, H. Q. Xu, and Z. Liu, Surface engineering of copper foils for growing centimeter-sized single-crystalline graphene, *ACS Nano* **10**, 2922 (2016).
- [40] See Supplemental Material at <http://link.aps.org/supplemental/10.1103/PhysRevB.101.085404> for more detailed numerical calculations, as well as theoretical analysis, which include Refs. [57–60].
- [41] S. Datta, *Electronic Transport in Mesoscopic Systems* (Cambridge University Press, Cambridge, 1995).
- [42] Y.-F. Chen, M.-H. Bae, C. Chialvo, T. Dirks, A. Bezryadin, and N. Mason, Magnetoresistance in single-layer graphene: Weak localization and universal conductance fluctuation studies, *J. Phys.: Condens. Matter* **22**, 205301 (2010).
- [43] R. Akis and D. K. Ferry, Closed versus open: To what extent do leads influence the magnetotransport in square quantum dots? *Semicond. Sci. Technol.* **13**, A18 (1998).
- [44] L. W. Molenkamp, A. A. M. Staring, C. W. J. Beenakker, R. Eppenga, C. E. Timmering, J. G. Williamson, C. J. P. M. Harmans, and C. T. Foxon, Electron-beam collimation with a quantum point contact, *Phys. Rev. B* **41**, 1274 (1990).
- [45] C. W. J. Beenakker and H. van Houten, Magnetotransport and nonadditivity of point-contact resistances in series, *Phys. Rev. B* **39**, 10445 (1989).
- [46] C. W. J. Beenakker, and H. van Houten, Quantum transport in semiconductor nanostructures, *Solid State Phys.* **44**, 1 (1991).
- [47] I. V. Zozoulenko, R. Schuster, K.-F. Berggren, and K. Ensslin, Ballistic electrons in an open square geometry: Selective probing of resonant-energy states, *Phys. Rev. B* **55**, R10209 (1997).
- [48] G. Q. Zhang, N. Kang, J. Y. Li, L. Lin, H. Peng, Z. Liu, and H. Q. Xu, Low-field magnetotransport in graphene cavity devices, *Nanotechnology* **29**, 205707 (2018).
- [49] R. Landauer, Electrical resistance of disordered one-dimensional lattices, *Philos. Mag.* **21**, 863 (1970).
- [50] F. Muñoz-Rojas, D. Jacob, J. Fernández-Rossier, and J. J. Palacios, Coherent transport in graphene nanoconstrictions, *Phys. Rev. B* **74**, 195417 (2006).
- [51] T. C. Li and S.-P. Lu, Quantum conductance of graphene nanoribbons with edge defect, *Phys. Rev. B* **77**, 085408 (2008).
- [52] P. R. Wallace, The band theory of graphite, *Phys. Rev.* **71**, 622 (1947).
- [53] S. Reich, J. Maultzsch, C. Thomsen, and P. Ordejón, Tight-binding description of graphene, *Phys. Rev. B* **66**, 035412 (2002).
- [54] A. Kretinin, G. L. Yu, R. Jalil, Y. Cao, F. Withers, A. Mishchenko, M. I. Katsnelson, K. S. Novoselov, A. K. Geim, and F. Guinea, Quantum capacitance measurements of electron-hole asymmetry and next-nearest-neighbor hopping in graphene, *Phys. Rev. B* **88**, 165427 (2013).
- [55] J. H. Bardarson, J. Tworzydło, P. W. Brouwer, and C. W. J. Beenakker, One-Parameter Scaling at the Dirac Point in Graphene, *Phys. Rev. Lett.* **99**, 106801 (2007).
- [56] M. Titov, Impurity-assisted tunneling in graphene, *Europhys. Lett.* **79**, 17004 (2007).
- [57] M. P. Sancho López, J. M. Sancho López, and J. Rubio, Quick iterative scheme for the calculation of transfer matrices: Application to Mo (100), *J. Phys. F* **14**, 1205 (1984).
- [58] J. P. Bird, R. Akis, D. K. Ferry, A. P. S. de Moura, Y.-C. Lai, and K. M. Indlekofer, Interference and interactions in open quantum dots, *Rep. Prog. Phys.* **66**, 583 (2003).
- [59] J. Xue, J. Sanchez-Yamagishi, D. Bulmash, P. Jacquod, A. Deshpande, K. Watanabe, T. Taniguchi, P. Jarillo-Herrero, and B. J. LeRoy, Scanning tunneling microscopy and spectroscopy of ultra-flat graphene on hexagonal boron nitride, *Nat. Mater.* **10**, 282 (2011).
- [60] J. Keski-Rahkonen, P. J. J. Luukko, S. Åberg, and E. Räsänen, Effects of scarring on quantum chaos in disordered quantum wells, *J. Phys.: Condens. Matter* **31**, 105301 (2019).